JACS
JOURNAL OF THE AMERICAN CHEMICAL SOCIETY

Article

pubs.acs.org/JACS

Solid Electrolyte Interphase Growth and Capacity Loss in Silicon Electrodes

Alison L. Michan,[†] Giorgio Divitini,[‡] Andrew J. Pell,[†] Michal Leskes,[†] Caterina Ducati,[‡] and Clare P. Grey*[,†]

[†]Department of Chemistry, University of Cambridge, Lensfield Road, Cambridge CB2 1EW, United Kingdom

[‡]Department of Material Science and Metallurgy, University of Cambridge, 27 Charles Babbage Road, Cambridge CB3 0FS, United Kingdom

Supporting Information

ABSTRACT: The solid electrolyte interphase (SEI) of the high capacity anode material Si is monitored over multiple electrochemical cycles by ^{7}Li, ^{19}F, and ^{13}C solid-state nuclear magnetic resonance spectroscopies, with the organics dominating the SEI. Homonuclear correlation experiments are used to identify the organic fragments $-OCH_2CH_2O-$, $-OCH_2CH_2-$, $-OCH_2CH_3$, and $-CH_2CH_3$ contained in both oligomeric species and lithium semicarbonates $ROCO_2Li$, RCO_2Li. The SEI growth is correlated with increasing electrode tortuosity by using focused ion beam and scanning electron microscopy. A two-stage model for lithiation capacity loss is developed: initially, the lithiation capacity steadily decreases, Li^+ is irreversibly consumed at a steady rate, and pronounced SEI growth is seen. Later, below 50% of the initial lithiation capacity, less Si is (de)lithiated resulting in less volume expansion and contraction; the rate of Li^+ being irreversibly consumed declines, and the Si SEI thickness stabilizes. The decreasing lithiation capacity is primarily attributed to kinetics, the increased electrode tortuosity severely limiting Li^+ ion diffusion through the bulk of the electrode. The resulting changes in the lithiation processes seen in the electrochemical capacity curves are ascribed to non-uniform lithiation, the reaction commencing near the separator/on the surface of the particles.

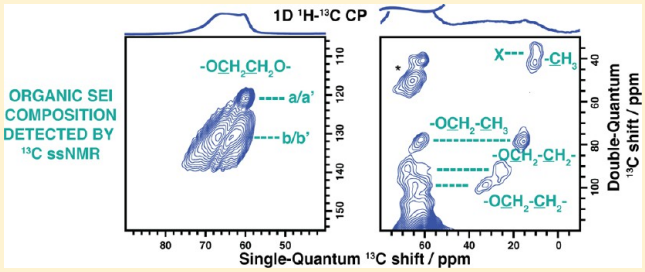

INTRODUCTION

In order for new electrode materials to be practically implemented in a Li-ion battery, sufficient capacity retention over many electrochemical cycles must be achieved. Since most negative electrode materials operate outside the electrochemical stability window of the electrolyte, this requires the formation of a stable solid electrolyte interphase (SEI) on the surfaces of the electrode so as to limit electrolyte breakdown.[1−7] In this study, we examine the electrode material Si, which forms an alloy with Li during electrochemical cycling. With its fully lithiated state of $Li_{15}Si_4$ corresponding to an excellent theoretical capacity of 3579 $mAhg^{-1}$, this material has the potential to improve the performance of Li-ion batteries.[8−10] However, to accommodate 15 Li per 4 Si atoms, a considerable volume expansion of up to 300% occurs during electrochemical cycling.[9,11,12] In contrast, the commonly used electrode material graphite, with a theoretical capacity of 372 $mAhg^{-1}$, has a much lower volume expansion of 10%.[9] The extreme volume expansion in Si systems, and other electrode materials forming Li alloys in Li-ion batteries, is thought to underlie their poor capacity retention; the volume expansion leads to mechanical failure and uncontrolled electrolyte decomposition preventing the formation of a stable SEI.[13,14]

With a fundamental understanding of the failure mechanisms in Si Li-ion battery systems, it may be possible to develop a successful strategy to achieve long-term capacity retention. Toward this goal, some strategies have already been explored. For example, the negative consequences of volume expansion may be mitigated using capacity-limited cycling, preventing the formation of the $Li_{15}Si_4$ phase.[15] The use of alternative Si morphologies may also be a way forward. For example, improved capacity retention has been achieved using Si nanowires, in part because these studies are performed at high rates, SEI formation depending strongly on the time the electrode spends at low voltages; electrical wiring of the nanowires to the current collector for the Si nanowires grown via chemical vapor deposition also aids retention.[16,17] Alternatively, the Si particle size can be reduced to nano particles; however, reducing the particle size leads to a greater surface area for electrolyte decomposition. Electrolyte additives are another strategy: Si systems cycled with electrolytes containing additives such as vinylene carbonate (VC) and fluoroethylene carbonate (FEC) show noticeably improved capacity retention.[18−20] These additive studies provide the motivation for a deeper understanding of the chemical composition and structure of what makes an optimal SEI. Toward this goal, we monitor the chemical composition and

Received: March 18, 2016
Published: May 27, 2016

DOI: 10.1021/jacs.6b02882
J. Am. Chem. Soc. 2016, 138, 7918−7931

growth of the SEI formed in a Si composite electrode system with a standard electrolyte (1 M $LiPF_6$ in ethylene carbonate (EC)/dimethyl carbonate (DMC)). A fundamental understanding of the failure mechanisms in this system will aid optimization of electrochemical cycling, electrode formulation, and the use of electrolyte additives.

Innovative experimental strategies can provide new insight, with the study of the SEI being impeded by the experimental challenges of probing the air sensitive,[21,22] amorphous, nanoscale-thick interface, which grows in situ during electrochemical cycling. In our previous study we employed solid-state NMR (ssNMR) using ^{13}C-labeled electrolyte solvents to probe the SEI formed in the first electrochemical cycle of C/Si binder-free composite electrodes.[23] In this study, we extend the ssNMR approach to multicycled electrodes containing 50 nm average particle size Si mixed with conductive C and a carboxymethylcellulose (CMC) binder, in order to monitor the growth of both the organic and inorganic components of the SEI. The local environments in the SEI are probed by ssNMR, ssNMR being a particularly advantageous technique in characterizing disordered systems, in contrast to other techniques such as X-ray diffraction (XRD). Furthermore, ssNMR is used to probe the bulk of the thick (up to approximately 100 nm) SEI layer in contrast to characterization techniques which are limited to the outermost layer of the SEI, such as X-ray photoelectron spectroscopy (XPS). Using ssNMR we can unambiguously detect chemically bonded environments relevant to the organic molecules and oligomers of the SEI. Additionally we examine the electrochemistry of the system and perform analysis of the electrode samples using focused ion beam (FIB) and scanning electron microscopy (SEM) characterization to observe the Si electrode pore structure and mechanical failure. The microstructure characterization complements the chemical analysis obtained by ssNMR and shows the relationship between SEI growth, electrode pore structure, and electrochemical capacity loss. Finally, we use electrochemistry to separately characterize the SEI formed on the conductive C in the system, demonstrating how capacity (loss) in the composite system may be influenced by the amount of conductive C in the formulation.

EXPERIMENTAL METHODS

^{13}C-Enriched Electrolyte Preparation. Enriched electrolytes were prepared in an Ar glovebox (typically H_2O and O_2 < 0.1 ppm) by dissolving 1 M lithium hexafluorophosphate $LiPF_6$ (Sigma-Aldrich, battery grade, ≥99.99%) in ethylene carbonate (EC) (Sigma-Aldrich, 97%, ^{13}C-labeled 99 atom %, and Sigma-Aldrich battery grade anhydrous, ≥99%, nonlabeled, ≤0.005% H_2O) and dimethyl carbonate (DMC) (Sigma-Aldrich, 97%, ^{13}C-labeled 99 atom % and Sigma-Aldrich, battery grade anhydrous, ≥99%, nonlabeled, ≤0.002% H_2O) 1:1 w/w. Both ^{13}C-labeled EC and nonlabeled battery grade EC were dried under vacuum in a mini-desiccator to remove any trace water, and transferred to an Ar glovebox. Both the ^{13}C-labeled DMC and battery grade DMC were dried using 4 Å molecular sieves to remove any moisture and transferred to an Ar glovebox. The dry DMC (<10 ppm of H_2O, by Metrohm 899 Karl Fischer Coulometer) was mixed with the dry nonlabeled battery grade EC and used to dilute the dried 99% enriched carbonates. 25% ^{13}C enriched electrolytes were prepared with either fully labeled ^{13}C EC or fully labeled ^{13}C DMC (Figure 1). Battery grade LP30 (1 M $LiPF_6$ in EC/DMC 1:1 v/v by Aldrich, ≤15 ppm of H_2O) was used when no isotope enrichment was required.

Electrode Formulation and Electrochemical Cycling. Crystalline Si powder (Sigma-Aldrich, average particle size 50 nm, <100 nm, ≥98%, 325 mesh) was mixed with Carbon SuperP (Timcal) and sodium carboxymethylcellulose (CMC) (Sigma-Aldrich, average

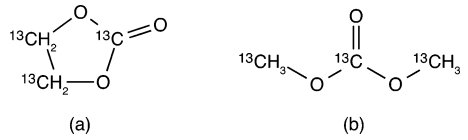

Figure 1. ^{13}C-enriched (a) EC and (b) DMC electrolyte molecules.

700 000 g mol^{-1}, 0.80–0.95 degree of substitution) in equal mass ratios (1:1:1) of 200 mg. A slurry was obtained by mixing the powders with 6 mL distilled water in a 70 mL stainless steel ball mill container using two 1/2 in. diameter balls for 30 min using a high energy Spex SamplePrep 8000M Mixer/Mill. The slurry was cast onto a copper substrate and dried at room temperature. Electrodes of 1/2 in. diameter were punched out of the dried film. These electrode samples were characterized using SEM and scanning transmission electron spectroscopy (S/TEM), seen in the Supporting Information, Figure S1; the Si particle oxidation layer is approximately 8–15 nm.

The electrodes were each dried for 2 h at 100 °C in a vacuum oven and then under dynamic vacuum in the prechamber of an Ar glovebox overnight before assembly into 2032 coin cells in an Ar glovebox (typically O_2 and H_2O < 0.1 ppm). The coin cell parts were dried with a minimum standard of 60 °C for a week followed by vacuum pumping in the prechamber of the Ar glovebox. The weight of the active material was approximately 0.5 mg per electrode, with each electrode individually weighed inside the glovebox prior to assembly. A counter electrode of Li metal (Sigma-Aldrich, Li metal ribbon, 0.38 mm thickness, 99.9%) was used. The Li metal counter electrode surfaces were cleaned using a soft brush before cell assembly. Standard porous glass fiber mat separators (Whatman GF/B) were saturated with electrolyte. An additional Celgard 2340 separator layer was used against the electrode surface to avoid any glass fiber sticking to the surface of the electrode samples.

The coin cells were galvanostatically cycled (using a Biologic VSP or MPG-2). The constant current discharge rate over 30 h, (C/X, X = 30 h) was calculated by $I = C_{Si}m_{Si}X^{-1}$, with m_{Si} being the mass of Si and C_{Si} being 3579 $mAhg^{-1}$ corresponding to the theoretical capacity of crystalline $Li_{15}Si_4$. The coin cells, prepared with enriched electrolytes, were cycled for 1, 30, and 60 cycles using voltage limits of 1 mV and 2 V. At the end of cycling, the coin cells were held at 2 V for 12 h. After cycling, the coin cells were disassembled under Ar and dried under dynamic vacuum in the prechamber of the glovebox. No solvent was used to rinse excess electrolyte from the samples to avoid any structural or compositional change to SEI grown on the electrode surfaces. The electrochemical data were processed using the Biologic EC-Lab V10.34 and Gnuplot V4.6 software.

Carbon SuperP powder electrodes, without Si and CMC binder, were assembled into coin cells using the same method as described for the Si composite electrodes. The conductive C was dried on a vacuum line at 100 °C for 2 days before being used in the 2032 coin cells in ∼1.5 mg quantities.

Solid State NMR. Ex situ multinuclear ssNMR spectra were obtained on 11.7 T Bruker Avance III 500 MHz and 9.4 T Bruker Avance 400 MHz spectrometers. Samples were packed under Ar, avoiding any exposure to ambient air, into rotors of 2.5 mm outer diameter. Magic-angle spinning (MAS) frequencies ranged from 10 to 30 kHz, spinning under N_2. Two to four electrode samples (of ∼1.5 mg) were combined to fill the rotors and enhance signal in the experiments. ^1H and ^{13}C chemical shifts were externally referenced to adamantane (^1H 1.9 ppm, ^{13}C 38.5 ppm, CH_2), and ^7Li and ^{19}F to LiF (^7Li −1 ppm, ^{19}F −204 ppm).[24,25] The data were processed using the Bruker TOPSPIN software and analyzed using the dmfit software.[26] Typical radio frequency (RF) field strengths used were (^1H) 135 kHz, (^7Li) 185 kHz, (^{19}F) 115 kHz, and (^{13}C) 125 kHz.

Samples prepared with each of the ^{13}C-labeled electrolyte solvents (Figure 1) were investigated by direct excitation ^{13}C, ^7Li, and ^{19}F ssNMR experiments to obtain quantitative information on the chemical environments. The ^{13}C spectra were acquired using swept-frequency two-pulse phase modulation (swfTPPM)[27] ^1H decoupling at 90–100 kHz. Two-dimensional (2D) cross-polarization (CP) ^{13}C

DOI: 10.1021/jacs.6b02882
J. Am. Chem. Soc. 2016, 138, 7918–7931

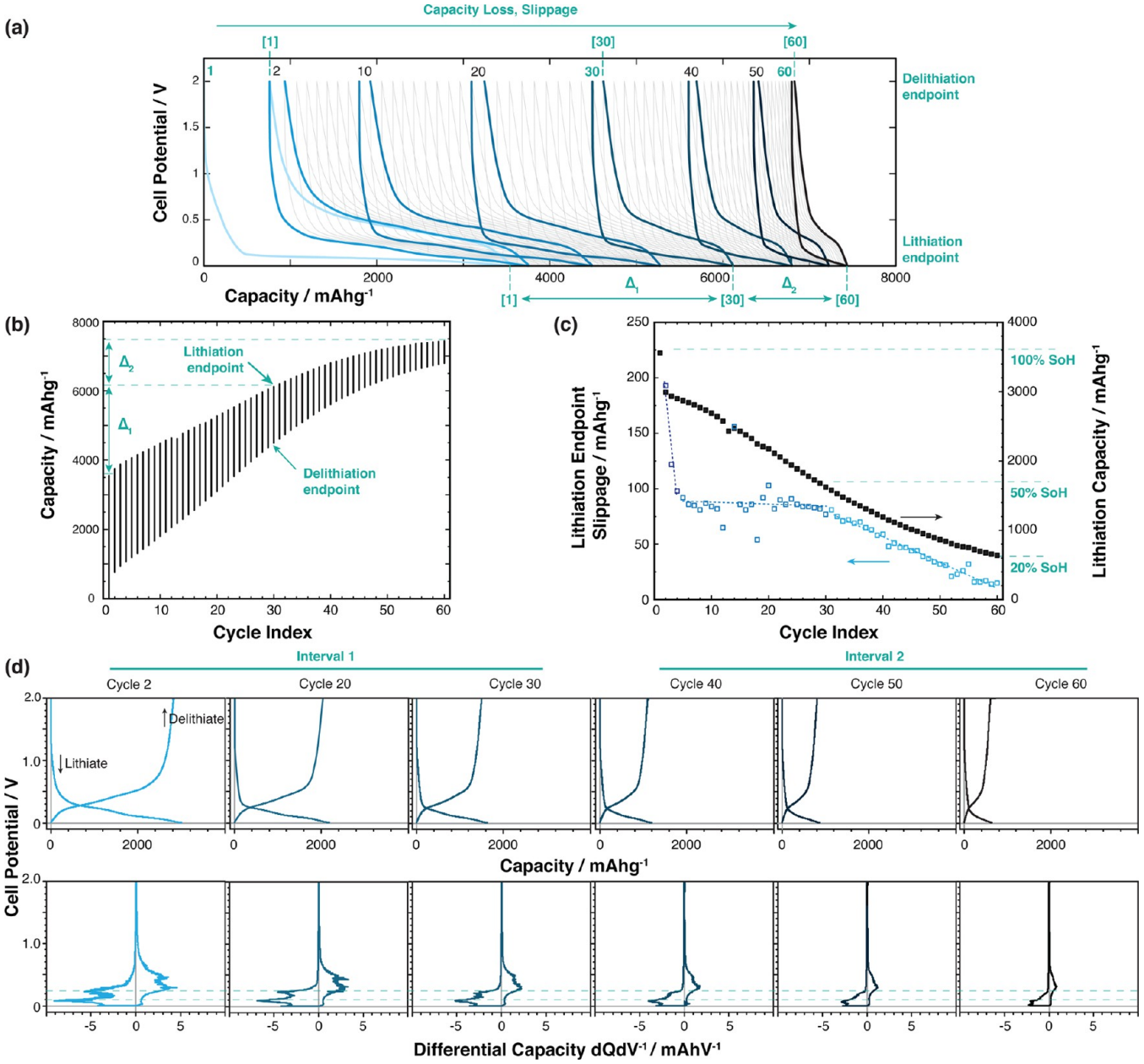

Figure 2. Electrochemical cycling of a Si/C/CMC composite electrode cycled against Li metal and plotted by (a) cell potential vs capacity and (b) capacity vs cycle index 1−60. In (c), the slippage (axis left, unfilled points) is compared to the lithiation/discharge capacity (axis right, filled points) for each cycle index. The slippage is approximated by three regions, indicated by linear fits. The lithiation endpoint slippage is defined as the difference of the lithiation endpoints for incremental cycles and is a measure of irreversibly consumed Li^+ in the system per cycle. Δ_1 and Δ_2 indicate the total irreversible capacity between cycles 1−30 and 30−60, respectively. In (d), selected capacity and differential capacity $dQ\,dV^{-1}$ curves for cycle 2−60 are presented, showing the detail of the lithiation/delithiation processes of the Si electrochemistry. Cycles 2−30 and 30−60 are labeled interval 1 and 2, respectively. Dashed lines indicate the initial potential of the electrochemical lithiation processes, occurring at approximately 250 and 100 mV.

homonuclear correlation experiments were performed, using a refocused INADEQUATE (Incredible Natural Abundance DoublE QUAntum Transfer Experiment) pulse sequence, to detect directly bonded C functional groups.[28−31] $^1H-^{13}C$ CP experiments were used to detect local environments with these nuclei in close spatial proximity by transferring magnetization from ^1H to ^{13}C nuclei. Dipolar dephasing (interrupted decoupling) $^1H-^{13}C$ cross-polarization experiments allowed differentiation between protonated and nonprotonated environments.[25,32]

Further experimental details are given in the Supporting Information.

SEM, FIB, and TEM. Electrode samples were transported from the Ar glovebox to the FIB and SEM instrument in sealed transport bags and transferred into the loading chambers with minimal ambient exposure (<5 min). Cross-sectional FIB/SEM was carried out in a FEI Helios Nanolab. A protective platinum layer was deposited onto the electrode surfaces prior to the FIB cuts to preserve surface structure. Milling was performed at 30 kV, with currents of ∼1 nA and ∼100 pA for rough cut and polishing steps, respectively. Due to the FIB/SEM geometry, SEM images were acquired at an angle of 38° from the surface.

Electrode samples were also characterized using S/TEM. A chemical map was obtained via electron energy-loss spectroscopy

DOI: 10.1021/jacs.6b02882
J. Am. Chem. Soc. 2016, 138, 7918−7931

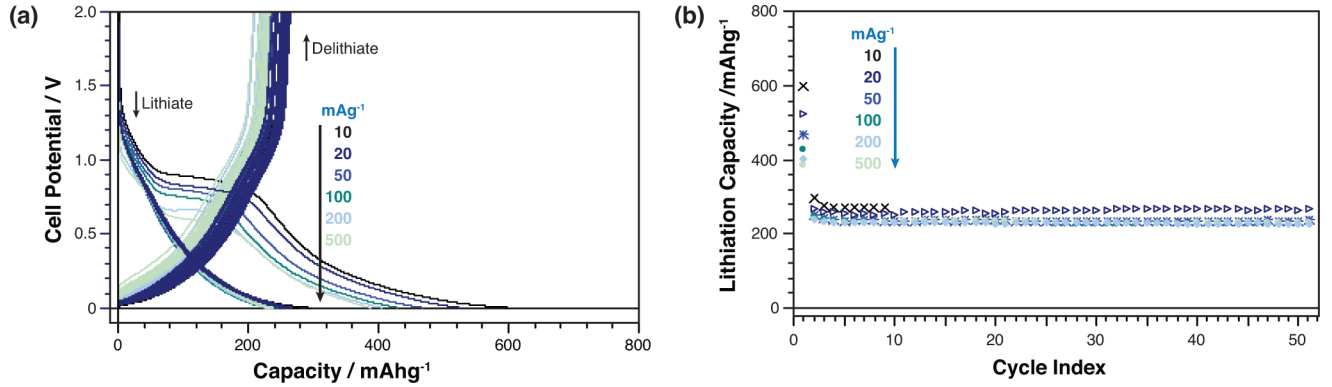

Figure 3. Electrochemical cycling of 6 coin cells with C SuperP powder electrodes cycled against Li metal. Capacities at constant currents of 10, 20, 50, 100, 200, and 500 mAg^{-1} were compared for 50 cycles plotted in (a) cell potential vs capacity (reset to 0 for each cycle) and (b) lithiation/discharge capacity vs cycle index. The result of (a) shows that the increasing current correlates with a decrease in the voltage, from approximately 0.9 down to 0.6 V, of the first electrolyte decomposition process. The result of (b) shows that the increasing current correlates with a decreasing lithiation/discharge capacity on the first cycle and stable capacity retention (in the absence of Si) from cycle 2 to 50.

(EELS) in a FEI Osiris S/TEM, operated at 200 kV, equipped with a Gatan Enfinium spectrometer.

RESULTS

Electrochemistry. The representative electrochemistry of a coin cell cycled 60 times is presented in Figure 2. This data took approximately 2.4 months of continuous galvanostatic cycling (constant current) to collect. The capacity over 60 cycles is demonstrated in panel (a) and is replotted as a function of cycle index in panel (b), with the lithiation and delithiation endpoints indicated. The difference between the capacity obtained on delithiation and lithiation, termed slippage,[33] is a measure of lost Li^+ in the system per cycle. The lithiation endpoint slippage for each cycle is compared to the lithiation capacity for each cycle in panel (c). Selected differential capacity curves are examined in panel (d).

In the first cycle, a lithiation/discharge capacity on the order of the theoretical capacity of Si (3579 $mAhg^{-1}$) was obtained, the first cycle lithiation capacity being assigned to 100% State of Health (SoH) (see cycle index 1 in panels a, b, c). Differences from the theoretical capacity of Si are ascribed to mass error and the fast current rate. A delithiation endpoint slippage (difference between discharge and charge capacity) of approximately 760 $mAhg^{-1}$ was accumulated (panel a). This capacity loss indicates Li^+ being irreversibly consumed in the first cycle, the chemical composition of the electrolyte decomposition products in the SEI at this delithiation endpoint being explored further by ssNMR.

We note that the delithiation/charge profile of the first cycle in panel (a) does not contain the characteristic delithiation plateau of the $Li_{15}Si_4$ phase indicating that this phase was not formed on lithiation. Recent studies have demonstrated that stress, either induced by the presence of a substrate in the case of Si films,[34] or internal stress in the case of alloys formed with an inactive component,[35] lowers the voltage at which the $Li_{15}Si_4$ phase is formed. These two studies suggest that the stresses induced by the inactive SiO_2 layer during expansion/contraction of the Si may similarly suppress $Li_{15}Si_4$ phase formation. However, this phase was observed following a hold step at low voltage combined with a slower cycling rate of C/75 in our previous study of a binder-free system,[23] and the electrochemical data of the binder-free system continuously cycled (provided in the Supporting Information, Figure S2), clearly shows the formation of this phase in the first few cycles; both results suggest that it is the increased polarization of the composite films that prevents $Li_{15}Si_4$ formation.

After 30 cycles, the lithiation endpoint was 6116 $mAhg^{-1}$ (see Figure 2 panels a and b). Δ_1, the total irreversible capacity for cycles 1−30, is approximately 2558 (6116−3558) $mAhg^{-1}$. The rate of this capacity loss is seen in panel (c), with the lithiation endpoint slippage of each cycle falling quickly in the first few cycles and then being relatively constant on the interval of cycle index 4 to 30. The near constant endpoint slippage occurring for each cycle indicates a steady rate of loss of Li^+ in the system. Higher precision instruments and improved environment control would likely improve the scatter of the data seen here.[36] Nevertheless, the broad trends of the slippage on the interval are seen. Simultaneously, the lithiation capacity, seen on the right-hand axis of panel (c), fell to approximately 50% SoH by cycle 30.

After 60 cycles, the lithiation endpoint was 7435 $mAhg^{-1}$ (see Figure 2 panels a and b). Δ_2, the total irreversible capacity for cycles 30−60, decreases to 1319 (7435−6116) $mAhg^{-1}$. The ratio Δ_1/Δ_2 is approximately 1.9; this ratio was analyzed for five samples and varies from approximately 1.7−1.9, likely due to mass error. The decrease in the total irreversible capacity on the interval Δ_2 compared to Δ_1 is attributed to the declining slippage trend of Δ_2 (see panel c), with the declining slippage indicating decreasing amounts of Li^+ being consumed irreversibly. The lithiation capacity continues to decrease on this second interval, reaching 20% SoH by cycle 60.

Representative electrochemical capacity and differential capacity curves in panel (d) provide additional insight. The second cycle shows two processes in the (de)lithiation curves, as expected for amorphous Si systems.[8,15,37−39] The two discharge/lithiation processes, indicating lithiation of amorphous silicon (a-Si+ xLi → a-Li_xSi and a-Li_xSi + x'Li → a-$Li_{(x+x')}Si$ with x and x' having values of approximately 2.0 and 1.5),[15,38] initially occur at approximately 250 mV and 100 mV. Based on our previous work,[10,38,39] the higher voltage process (250 mV) corresponds to the initial lithiation of amorphous Si and subsequent breaking apart of the amorphous Si into large Si clusters by the Li insertion. The lower voltage process (100 mV) corresponds to further Li reaction with the increasingly smaller Si clusters, e.g., Si−Si dimers, eventually resulting in only isolated Si anions at approximately ($Li_{3.5}Si$). Between cycle 20 and cycle 30 the intensity of the high voltage (250 mV) peak

DOI: 10.1021/jacs.6b02882
J. Am. Chem. Soc. 2016, 138, 7918−7931

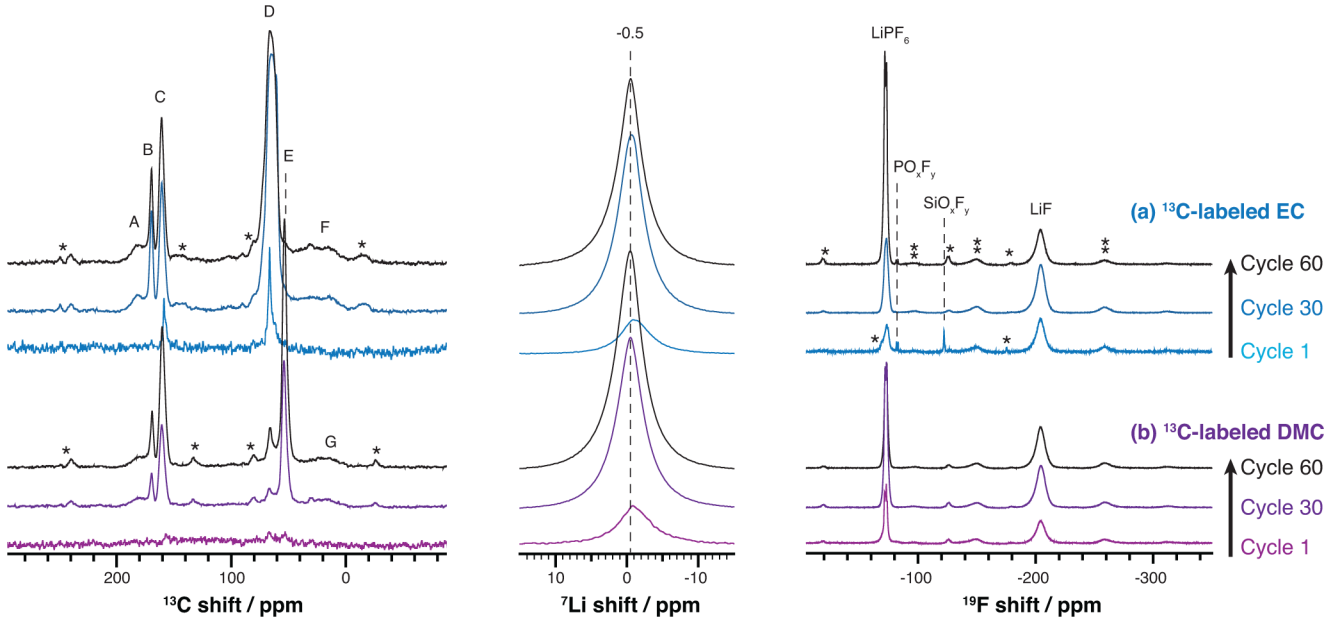

Figure 4. Direct excitation ^{13}C, ^{7}Li, and ^{19}F ssNMR experiments of electrode samples prepared with (a) ^{13}C EC (blue) and (b) ^{13}C DMC (purple) labeled electrolytes. Measurements were performed on electrode samples from coin cells cycled through 1, 30, and 60 electrochemical cycles (approximately 100, 50, 20% SoH). Single pulse ^{13}C and Hahn echo ^{19}F spectra were acquired on a 500 MHz spectrometer with 10 and 25 kHz MAS rate, respectively. ^{7}Li single pulse spectra were acquired on a 400 MHz spectrometer with 30 kHz MAS rate. ^{13}C peak assignments A–G are summarized in Table 1. Asterisks indicate spinning side bands.

in the differential capacity plots becomes less pronounced and by cycle 40 is barely visible (indicated by the top dashed line in panel d). Interestingly, the decreased intensity of this high voltage process is seen for both the lithiation and delithiation (discharge and charge) showing that this change is symmetric.

The electrochemical profiles are approximated by two intervals, cycles 2–30 (100–50% SoH) and cycles 30–60 (50–20% SoH). In the first interval, all the Si lithiation processes are evident, and Li^+ is irreversibly consumed at a steady rate. In the second interval, the Si lithiation processes are less evident, and less irreversible capacity is accumulated. The decreasing rate of Li^+ being irreversibly consumed is correlated with a decreasing amount of lithiation of the Si particles in the system, and thus both the reduced volume expansion of the electrode and the time the electrode spends at low potentials.

Additional experiments were performed to explore the cell failure further. In the first experiment (see Supporting Information Figures S4 and S5), an electrode sample was cycled for 60 cycles at a constant current of $C/30$ and then the current was reduced by a factor of 10 to $C/300$. The experiment showed a recovery of lost lithiation capacity at the slow current and the high voltage lithiation/delithiation processes reappeared. These results suggest that kinetics are a clear factor contributing to the lithiation capacity fade. In a second experiment, a cell was stopped at the lithiation endpoint on cycle 60 and disassembled to confirm that sufficient Li metal was available and that the separator was still soaked with electrolyte. Contributions from surface effects on the Li metal to slippage and discharge capacity loss cannot be ruled out, but they cause slippage in the opposite direction.

To characterize the lithiation capacity relating to the conductive C in the system, 6 C SuperP electrodes were cycled against Li metal in coin cells with constant currents from 10 to 500 mAg^{-1} (Figure 3). An initial lithiation capacity up to ~600 $mAhg^{-1}$ was obtained at the lowest current of 10 mAg^{-1}, dropping to ~400 $mAhg^{-1}$ at the highest current of 500 mAg^{-1} (compared to C/30 and 119 mAg^{-1} for the composite Si electrodes). The decreasing potential of the pseudo plateau in the first cycle is clearly a polarization effect. With a C SuperP:Si 1:1 mixture in the composite electrode system, approximately 400 $mAhg^{-1}$ of the capacity in the first cycle is attributed to the presence of C SuperP. An irreversible capacity in the first cycle of ~200 $mAhg^{-1}$ (see Supporting Information, Figure S3) is likely due to SEI formation on conductive C surfaces. Note that this approximation does not take into account the effects of the binder or electrode formulation. Clearly, the expansion of Si and the composite electrode formulation would have an impact on the capacity retention relating to the conductive C in the system. But in the absence of Si, a stable lithiation capacity from the C-only electrodes of approximately ~230 $mAhg^{-1}$ was measured.

SEI Growth Measured by ssNMR. With the capacity loss observed by electrochemistry, the corresponding SEI growth was monitored using ssNMR on samples prepared at the delithiation point after cycle 1, 30, and 60. Quantitative signal intensities were obtained by performing direct excitation ^{13}C, ^{7}Li, and ^{19}F ssNMR experiments (Figure 4) for each of the ^{13}C-labeled EC and DMC sample sets. Each of the samples consist of 2–4 individual electrode samples, which were combined for the ssNMR experiments; any minor variations between cycled electrode samples are therefore averaged. The experimental data and analysis presented here are supported by detailed analysis and additional ssNMR spectra, available in the Supporting Information: experiments with varying MAS rates confirm the position of the ssNMR spinning side bands (indicated by asterisks in Figure 4), while control measurements on the CMC binder and pristine electrode material confirm the chemical shifts of carbon functional groups that are attributed to the electrode material rather than to the SEI.

^{19}F ssNMR. The ^{19}F ssNMR results show resonances assigned to LiF (−204 ppm) and residual $LiPF_6$ (−73 ppm)

DOI: 10.1021/jacs.6b02882
J. Am. Chem. Soc. 2016, 138, 7918–7931

in the system (Figure 4). In the cycle 1 and 30 ^{13}C-labeled EC samples, sharp resonances are seen at −84 and −122 ppm. The −84 ppm resonance is assigned to PO_xF_y species such as Li_xPOF_y, with these species being formed by reactions with H_2O and PF_x decomposition products of $LiPF_6$.[40] The −122 ppm resonance has a chemical shift in the range of SiO_xF_y species,[41] such species having been detected on the surfaces of Si by Philippe et al. using photoelectron spectroscopy.[42] The presence of F−C bonds, also resonating in this region of the ^{19}F spectra, were ruled out by ^{19}F−^{13}C CP experiments (see the Supporting Information). The amount of LiF (indicated by the integrated intensity of the −204 ppm peak) does not increase significantly after the first cycle, suggesting that LiF is formed primarily in the initial cycle. The amount of residual $LiPF_6$ salt varies between the samples, with an increased amount of residual $LiPF_6$ salt being seen after the first cycle in each of the ^{13}C-labeled EC and DMC sample sets. The results are consistent with $LiPF_6$ salt being trapped in the SEI, the thickness of the SEI layer increasing during cycling. An evolving pore structure may also trap more residual electrolyte.

^{7}Li ssNMR. The overall ^{7}Li signal intensity increases with cycle number in both sample sets, the most pronounced increase occurring in the first 30 cycles (Figure 4). After the first cycle, the broad ^{7}Li resonance is centered at approximately −1.0 ppm (the chemical shift of LiF) and after subsequent cycles the resonance shifts to approximately −0.5 ppm. The broad −0.5 ppm resonance is assigned to Li salts including LiF (−1.0 ppm), Li_2CO_3 (0.0 ppm), $ROCO_2Li$, $LiPF_6$ (−2.9 ppm), and possibly Li_4SiO_4 (1.2 ppm).[43−45] The low resolution of the ^{7}Li ssNMR spectra impedes accurate deconvolution of the Li salt environments. However, these ^{7}Li assignments are supported by the ^{19}F and ^{13}C ssNMR spectra which have a much larger chemical shift dispersion.

^{13}C ssNMR. The growth of the organics of the SEI is evident by the increasing signal intensities seen in the spectra in Figure 4, between cycle 1 and cycle 30, the ^{13}C resonances in each of the ^{13}C-labeled EC and DMC samples being labeled A−G. The organic SEI composition is further investigated by 2D ^{13}C homonuclear correlation (INADEQUATE)[28−31] and cross-polarization ssNMR experiments in Figures 5 and 6. Any residual EC remaining in the electrodes is not observable in the 2D ^{13}C INADEQUATE ssNMR experiment of Figure 5 as the CH_2 ^{13}C nuclei are magnetically equivalent. For each of the samples, similar environments are observed in the carbonate and carboxyl region (A, B, C). The overlapping resonances contributing to D/F and E/G are characteristic of EC and DMC decomposition products, respectively.[23] The integrated signal intensity between the 30 and 60 cycles is approximately equal, with quantitative error arising from residual electrolyte, and differences in the sample mass packed inside the ssNMR rotors. An additional error may arise from the undesired removal of a small fraction of the SEI at the surface of the electrode, which may adhere to the separator instead of the electrode when they are physically separated during battery disassembly. A deconvolution analysis was performed for a more quantitative comparison (see Supporting Information Table S1). To improve accuracy, the Gaussian fits corresponding to resonances C, D, and E, were excluded from the integrated signal intensity, thereby removing any error arising from residual EC and DMC (the assignments are discussed further, see Table 1). The ratios of the integrated signal intensities of the samples at cycle 60/cycle 30 of 1.2 and 1.1 were found for the ^{13}C-labeled DMC and EC samples,

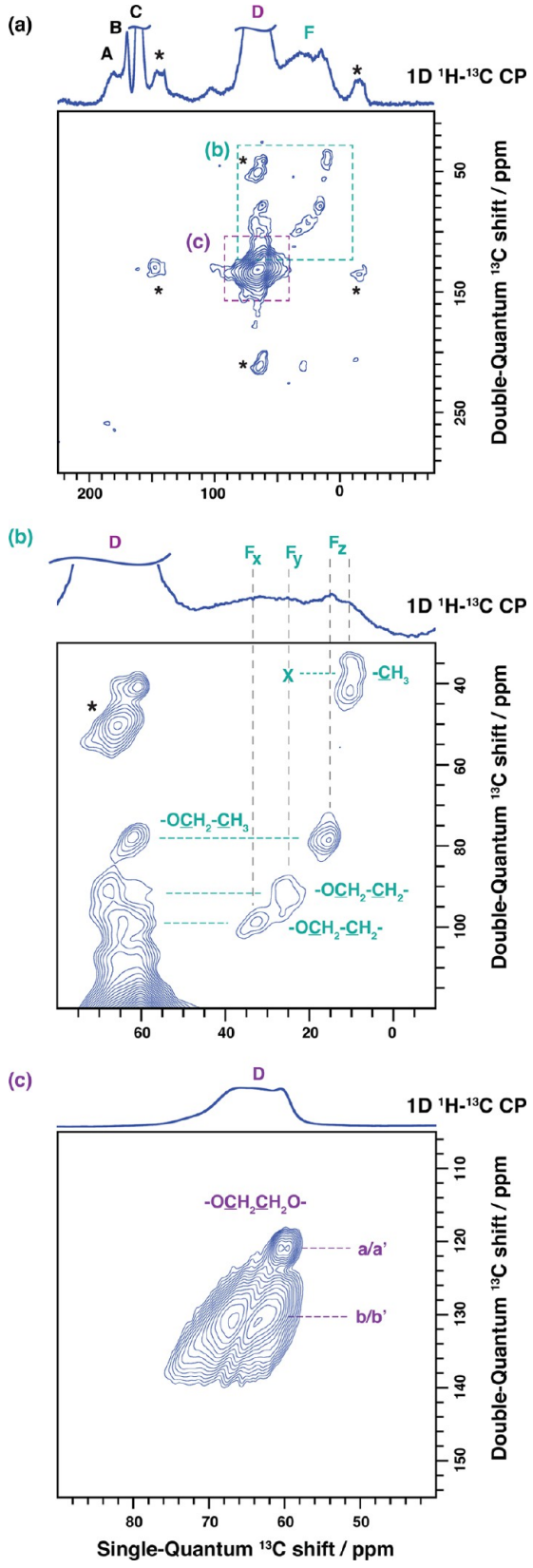

Figure 5. ^{13}C DQ/SQ homonuclear correlation ssNMR experiment performed on the 30 cycle sample prepared with ^{13}C-labeled EC electrolyte. The correlations in the J-based ^{1}H−^{13}C CP refocused INADEQUATE experiment show the pairs of resonances which are bonded. See the Supporting Information for views of the spectra with lower contour levels. Asterisks indicate spinning sidebands.

DOI: 10.1021/jacs.6b02882
J. Am. Chem. Soc. 2016, 138, 7918−7931

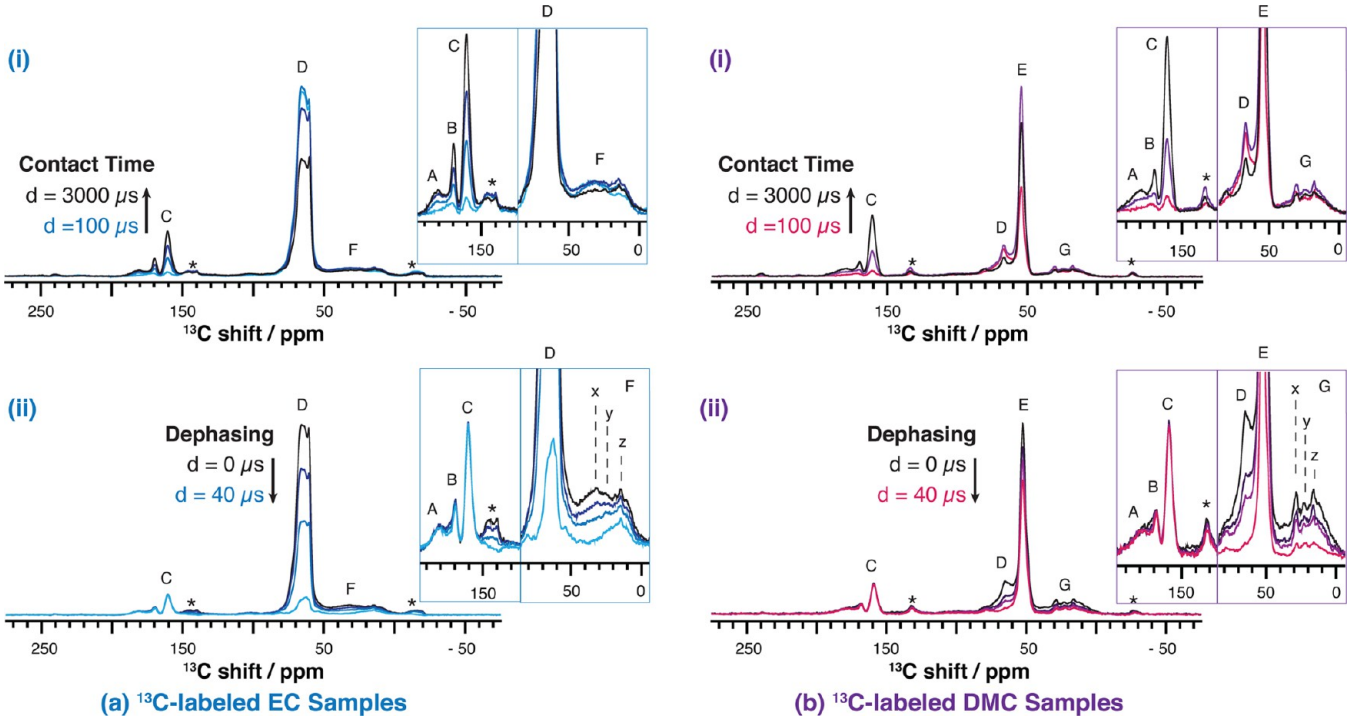

Figure 6. ssNMR $^{1}H-^{13}C$ cross-polarization and dephasing experiments of electrode samples prepared with (a, left) ^{13}C EC and (b, right) ^{13}C DMC labeled electrolytes. When delay times are varied in the experiment, different carbon functional groups can be identified based on their attenuation rates. In (a-i, b-i), CP contact times in the experiments were varied, and in (ii-a, ii-b) dephasing times were varied. See the Supporting Information for ssNMR pulse sequence details. Increasing CP contact times of (a-i) 100, 500, 1000, 3000 μs and (b-i) 100, 500, 3000 μs correlate with increasing carbonate and carboxyl signal intensities. Using a fixed CP contact time of 500 μs, increasing dephasing times of (a-ii) 0, 10, 15, 40 μs and (b-ii) 0, 15, 20, 30 μs correlate with decreasing signal intensities of proton-bonded carbons. Asterisks indicate spinning sidebands.

Table 1. Summary of ^{13}C ssNMR Assignment of Carbon Functionalities A–G in Figures 4–6[a]

resonance	^{13}C shift/ppm	fragment
A: EC/DMC	179	R$\underline{C}O_2$Li, H$\underline{C}O_2$Li/$CH_3CH_2\underline{C}O_2$Li
B: EC/DMC	170	$Li_2\underline{C}O_3$
C: EC/DMC	160	RO$\underline{C}O_2$Li, residual EC/DMC $\underline{C}$=O
D: EC/DMC	67	$\underline{R}OCO_2$Li, $-O\underline{C}H_2\underline{C}H_2O-$ residual EC O$\underline{C}H_2$
E: DMC	53	$\underline{C}H_3OCO_2$Li, residual DMC O$\underline{C}H_3$
$\mathbf{F}_x$: EC	30	R$\underline{C}H_2$R′
$\mathbf{F}_y$: EC	23	$CH_3\underline{C}H_2$R
$\mathbf{F}_z$: EC	14	$\underline{C}H_3$R
$\mathbf{G}_x$: DMC	30	R$\underline{C}H_2$R′
$\mathbf{G}_y$: DMC	23	$CH_3\underline{C}H_2$R
$\mathbf{G}_z$: DMC	14	$\underline{C}H_3$R

[a]Specific R-groups are suggested where possible. The assignments in Table 1 are based on our previous assignments.[23]

respectively, indicating that while the majority of SEI growth has already occurred by cycle 30 (50% SoH, Figure 2b) in these samples, there is a minor growth of 10–20% of the organics in the SEI. This is noticeably less than might be expected from the analysis of the endpoint slippages Δ_1/Δ_2 (Figure 2b) where an average ratio of 1.7–1.9 was found, which would translate into an increase in the integrated signal intensities on the order of 50–60% if all the irreversible capacity loss would have resulted in the formation of a solid SEI. Furthermore, no new chemical environments are detected between 30 and 60 cycles, in any of the ^{19}F, ^{7}Li, or ^{13}C ssNMR spectra. The result suggests that additional factors beyond SEI growth contribute to the endpoint slippage. For example, soluble SEI products contained in the electrolyte are not accounted for in the ssNMR result here, the solubility of the SEI having been investigated by others.[46] It is also worth noting that if the SEI increasingly forms at the surface of the electrode, then any error induced by SEI adhering to the separator would decrease the signal intensity of the cycle 60 sample more than the cycle 30 sample.

The large chemical shift dispersion of the ^{13}C spectra allows for definitive assignment of the carbon functional groups present in the 30 and 60 cycle samples. The ^{13}C NMR spectra strongly resemble that of our previous study of the SEI composition of a binder-free system after 1 cycle. The carboxyl resonance A (179 ppm) indicates an R$\underline{C}O_2$Li environment. While additional species cannot be ruled out, H$\underline{C}O_2$Li and $CH_3CH_2\underline{C}O_2$Li represent the most likely species; the presence of H$\underline{C}O_2$Li was confirmed by ^{1}H NMR (see Supporting Information Figure S13). The carbonate resonance B (170 ppm) is assigned to $Li_2\underline{C}O_3$ based on its distinctive chemical shift. The distribution of carbonate environments giving rise to the peak labeled C (160 ppm) includes RO$\underline{C}O_2$Li decomposition products, and some minor contribution from the carbonate environments of residual EC and DMC. The distribution of sp^3 carbons contributing to resonance D (67 ppm) are characteristic of $\underline{R}OCO_2$Li and $-O\underline{C}H_2\underline{C}H_2O-$ oligomer environments, expected decomposition products of EC. Some minor contribution from residual EC O$\underline{C}H_2$ groups (67 ppm) also contribute to D. The resonance labeled E is assigned to $\underline{C}H_3OCO_2$Li, lithium methyl carbonate (LMC), with some minor contribution from residual DMC O$\underline{C}H_3$ groups. The resonances labeled F and G (0–50 ppm) have chemical shifts characteristic of CH_3 and CH_2 environments

DOI: 10.1021/jacs.6b02882
J. Am. Chem. Soc. 2016, 138, 7918–7931

which are not adjacent to O atoms. Furthermore, the very broad line shape of resonances F and G are a clear signature of amorphous/disordered environments. The distribution of environments is approximately described by three representative shifts of 30, 23, and 14 ppm (labeled by subscripts *x*, *y*, *z* in Figures 5b and 6ii). In previous work, we explored chemical shift trends of expected SEI molecules using DFT calculations.[23] Based on our initial NMR chemical shift map of the organics in the SEI we expect $\underline{C}H_3R$ environments, present in SEI molecules such as RCO_2Li, to resonate at lower chemical shifts of approximately 15 ppm. $CH_3\underline{C}H_2R$ environments are expected to resonate at higher shifts of approximately 20 ppm. $R'\underline{C}H_2R$ environments, present in molecules such as lithium butylene dicarbonate (LBDC), are expected to resonate at higher shifts of approximately 25−30 ppm. However, we note many molecules or fragments may form and contribute to the signal in this region.

SEI Organic Composition, ^{13}C ssNMR. The region of the ssNMR spectra of resonances D−G are of interest in determining the length and composition of the alkyl chains of the SEI organics. These environments were examined using a 2D ^{13}C homonuclear correlation experiment (INADEQUATE).[28−31] This experiment shows correlations between directly bonded ^{13}C resonances with different chemical shifts and excludes all nonbonded ^{13}C resonances. The result of the experiment performed on the 30-cycle ^{13}C-labeled EC sample is shown in Figure 5. With the CH_2 groups of EC being magnetically equivalent, any detection of residual EC is excluded. The complementary 2D ssNMR experiment performed on the ^{13}C-labeled DMC sample is contained in the Supporting Information, Figure S8.

Figure 5 panel (a) shows the overall spectrum showing correlations involving OCH_2 (resonance D) and CH_2/CH_3 (resonance F) groups. Panel (b) shows an expansion of part of the spectrum, more clearly showing these D−F correlations. While many correlations might be expected, only the unambiguous correlations are labeled. These correlations correspond to OCH_2 resonances D bonded with F_x (CH_2, 30 ppm), F_y (CH_2, 23 ppm), and F_z (CH_3, 14 ppm). An additional CH_3 correlation is also seen at 10 ppm and based on its double-quantum frequency is expected to correlate with a CH_2 group (23 ppm), (indicated by a dashed line and "X"). The lack of signal in the 23 ppm (CH_2) region is tentatively ascribed to the faster dephasing and subsequent signal loss during the ssNMR pulse sequence of a CH_2 group vs a CH_3 group. These bonded environments are present in SEI decomposition products such as LBDC, RCO_2Li, and lithium ethylene carbonate (LEC). The detection of these correlations is limited by the inherent sensitivity of the experiment and additional correlations are likely to be present: views of panels (a) and (b) with lower contour levels are presented in the Supporting Information, Figure S9, showing these additional correlations. Panel (c) is an expansion of the resonance D region, showing correlations between different CH_2O groups. The correlations clearly indicate at least two $-OCH_2CH_2O-$ fragments corresponding to C pairs within different molecules or within the same molecule, separated from the rest of the alkyl chain by an O. These fragments are contained in poly(ethylene oxide) (PEO) type oligomers, and lithium alkyl (di)carbonates.

The nature of the different environments were more rigorously investigated using $^1H-^{13}C$ cross-polarization (CP) ssNMR experiments (Figure 6), with the signal intensity in these experiments depending on molecular dynamics, mobility, and spatial proximity of ^1H and ^{13}C nuclei. In one set of experiments (a-i, b-i) the CP contact time in the experiment was varied, showing an increasing signal intensity in the carbonate and carboxyl region of the spectra (resonances A−C) with increasing CP contact time (see inset, left). In contrast, the environments labeled D and E begin to attenuate in the experiment, due to signal loss during the longer CP contact times (due to shorter dephasing times of the spin-locked magnetization in the CP pulse sequence, defined by the NMR parameter $T_{1\rho}$). The maximum signal intensity of D and E are observed at 500 μs. By 3000 μs the signal intensities of D are attenuated to approximately 50% of the signal intensity maximum, and the overlapping resonances labeled E is attenuated to approximately 75% of the signal intensity maximum. This observed behavior is characteristic of CH_2 and CH_3 environments, respectively. Overlapping resonances labeled F and G also show some minor attenuation.

In a second set of experiments (a-ii, b-ii) a delay was introduced, following the cross-polarization step in the experiment, to perform a dipolar dephasing (interrupted decoupling) experiment (see the Supporting Information for experimental details). This experiment allows protonated and nonprotonated environments to be differentiated, the signal intensities of the CH and CH_2 groups attenuating more rapidly in comparison to the signals from nonprotonated carbon. Mobility of the CH_x environments is also probed, with rigid CH/CH_2 environments attenuating more rapidly than signal from mobile species such as rotating CH_3 methyl groups (due to a reduced dipolar coupling). Note that the dephasing times differ slightly between the two samples (a, b) and that the broad resonances F and G are visually skewed by the overlapping dephasing of D and E (in each of a-ii, b-ii). The carboxyl and carbonate resonances A−C, which do not have directly bonded protons, are not attenuated in the experiment (see inset, left). In contrast, the overlapping resonances of D show a pronounced attenuation with increasing dephasing times in each of the experiments, characteristic of CH_2 functional groups (see inset, right): by 15 μs dephasing delay in each of the samples, D is attenuated to approximately 50% of its maximum signal intensity. Resonance E shows less rapid attenuation than D, characteristic of CH_3 functional groups, dropping to only approximately 80% of its maximum signal intensity following a 15 μs dephasing delay in the ^{13}C-labeled DMC sample. Additionally, the dephasing experiments confirm multiple environments in the 0−50 ppm range. Within the broad resonances F and G, the environments with higher chemical shifts, F_x/G_x (30 ppm), attenuate the most rapidly, characteristic of CH_2 functional groups (marginally slower than D). The environments with a lower chemical shift, F_z/G_z (14 ppm) attenuate the least rapidly, characteristic of CH_3 functional groups (comparable to E). Covalent bonding with the C functional groups seen in the dephasing experiment were confirmed in the ^{13}C homonuclear correlation ssNMR experiment (Figure 5).

Surface and Pore Structure Analysis. Analysis of the electrode surfaces before and after cycling shows evidence of mechanical failure, with electrode cracking of the films being seen at different length scales, from ~100 μm down to ~1 μm, Figure 7. The cracking is likely due to the large Si expansion and contraction during cycling.

SEM views of FIB cross sections show the changing pore structure of the electrode after electrochemical cycling, Figure 8. The initial structure of the pristine electrode, before cycling

DOI: 10.1021/jacs.6b02882
J. Am. Chem. Soc. 2016, 138, 7918−7931

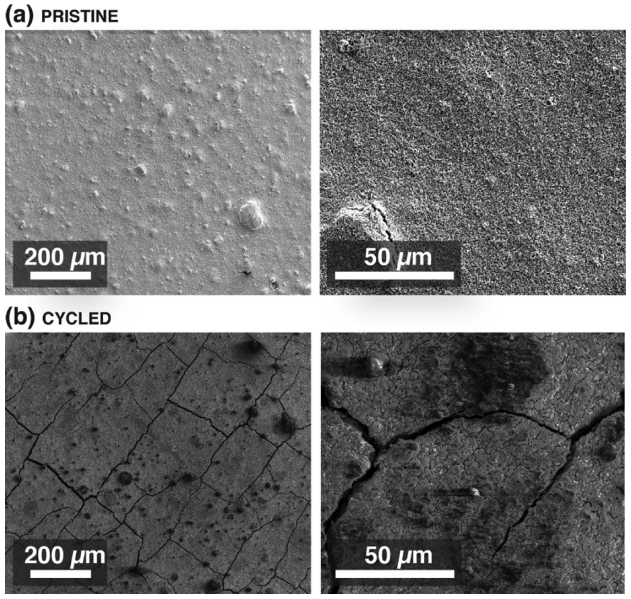

Figure 7. SEM images of a (a) pristine uncycled electrode and (b) cycled electrode sample, after 60 electrochemical cycles.

and assembly, has a relatively low density, with roughly spherical pores, starting in size from a few tens of nm, between Si and C particles, panel (a). After one electrochemical cycle, panel (b), the electrode displays a higher density due to some aggregation of particles into larger solid structures; fewer small, spherical pores are observed, and larger voids dominate the overall pore morphology. A control experiment confirmed no structural change was caused by the residual electrolyte and assembly into a coin cell; see the Supporting Information for a comparison of an electrode sample that was assembled and wet with electrolyte, compared to the pristine electrode sample that was neither assembled nor wet with electrolyte. By 30 and 60 cycles, panels (c) and (d), the electrode has a much higher density, with further agglomeration of particles. Some very large voids, up to several hundreds of microns, are still visible, but the overall structure is considerably more compact than in the pristine case. The 60 cycle sample shows some larger voids than the 30 cycle sample and evidence of more pore clogging. However, the overall microstructure of the 30 and 60 cycle samples are very similar within the error and sampling statistics of the experiments. The similar pore structures observed by FIB/SEM for the 30 and 60 cycle samples are in agreement with the ssNMR results, which detect similar quantities of SEI on the same interval.

The electrode sample at cycle 60 was examined at higher resolution. An analysis region is indicated in panel (e), centered on a large void in the electrode sample, which may have formed due to a gas bubble formed during the electrode preparation. The void allows for views in panels (f–h) of the complex pore structure formed by Si and C particles, with distance from the FIB cut and away from any possible damage from the FIB process. Examining the high resolution images closely, lighter contrast regions are observed on some of the particle agglomerates, which have approximately 100 nm thickness (see panel h). With the growth of the SEI already detected by ssNMR (Figures 4–6), these lighter contrast regions likely indicate SEI on particle surfaces.

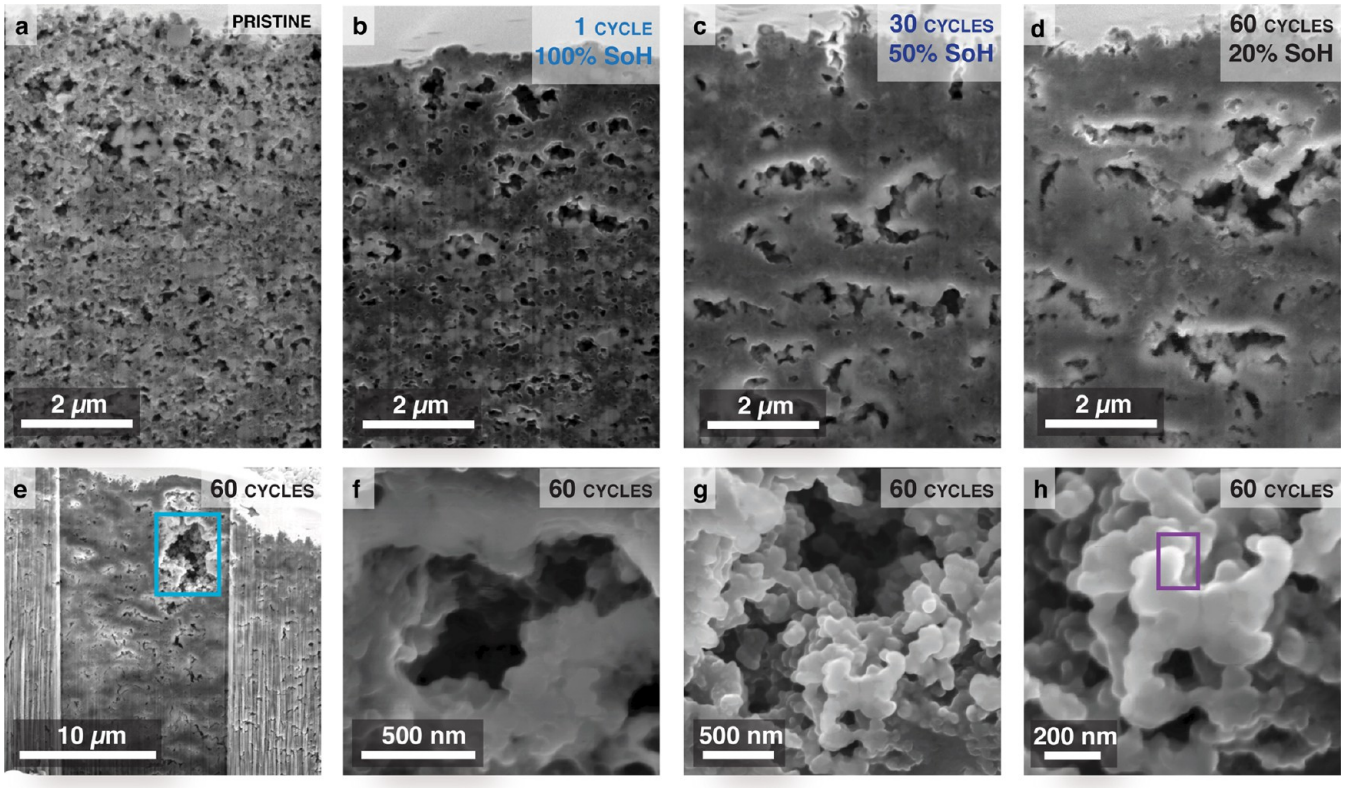

Figure 8. (a–d) SEM images of FIB cross sections, showing the pore structure of the electrodes after 0, 1, 30, and 60 electrochemical cycles. (e) Analysis region for (f, g, h). High magnification views of an electrode after cycle 60 (20% SoH) (f, g, h) shows evidence of SEI growth (see h) on the C and Si particle surfaces of the electrode.

DOI: 10.1021/jacs.6b02882
J. Am. Chem. Soc. 2016, 138, 7918–7931

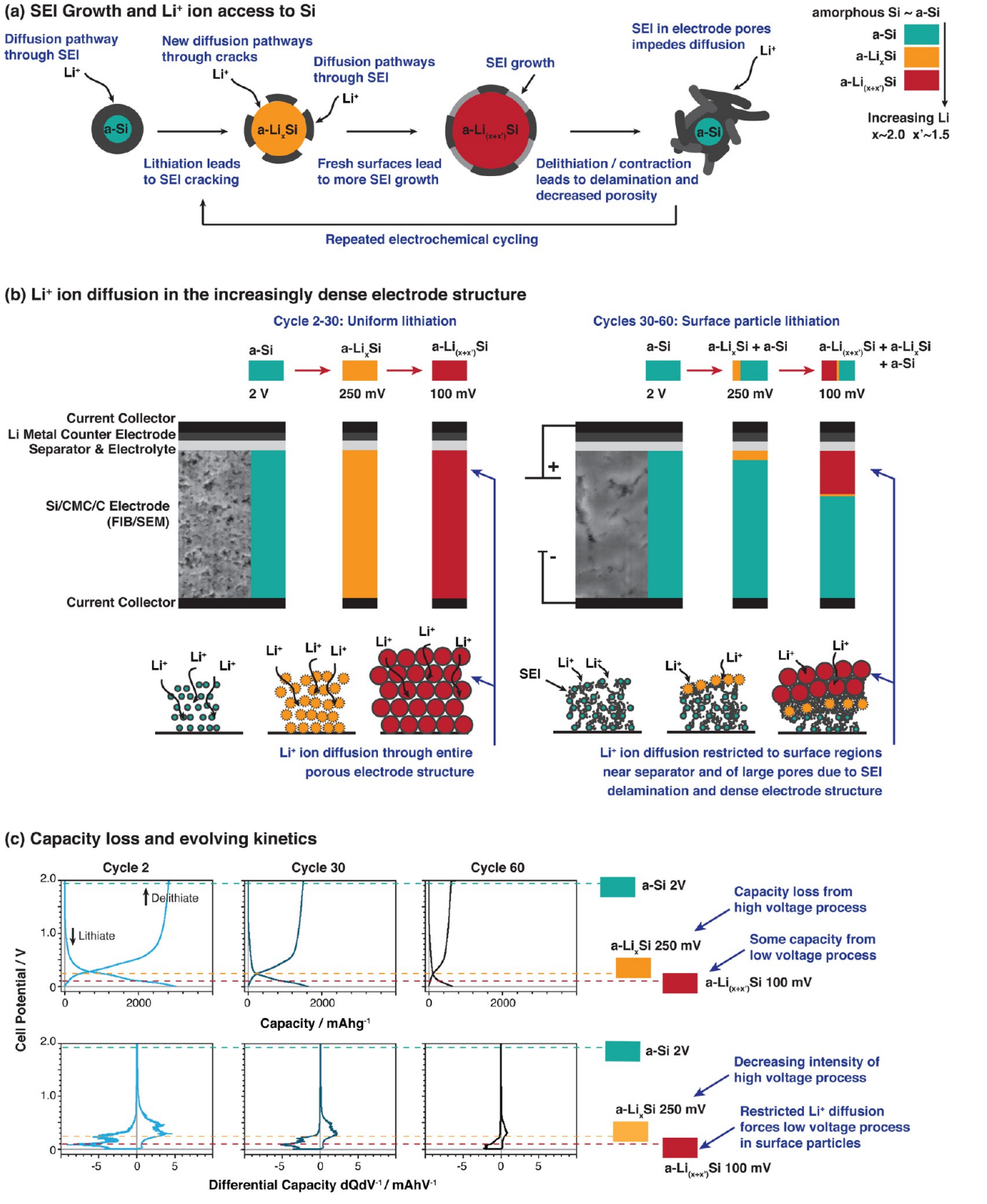

Figure 9. Multilength scale model of SEI growth and Li^+ ion diffusion as failure mechanisms for a Si composite electrode, electrochemically cycled in a half-cell configuration against a Li metal counter electrode. (a) Schematic showing nanoscale processes: Li^+ ion diffusion through cracks in the SEI, additional SEI growth, and delamination from Si particle surfaces. (b) Schematic showing microscale processes: electrode pore structure becomes more dense, restricting Li^+ diffusion to surface regions near the separator and to surface regions of large pores formed due to particle agglomeration and mechanical stresses. The FIB/SEM (from Figure 8) electrode cross sections show the increasing density of the electrode pore structure. Note that the carbon and binder are omitted from the cartoon below the FIB/SEM cross sections for clarity, the true electrode structure being more dense than implied. (c) Atomic scale processes: Si electrochemistry (from Figure 2c) at cycle 2, 30, and 60, highlighting the evolution of the higher (250 mV) and lower (100 mV) voltage amorphous Si lithiation processes and corresponding capacity loss.

DOI: 10.1021/jacs.6b02882
J. Am. Chem. Soc. 2016, 138, 7918−7931

DISCUSSION

An irreversible capacity of 760 $mAhg^{-1}$ was measured by electrochemistry in the first cycle, which corresponds to approximately 10% of the overall endpoint slippage accumulated following 60 cycles (Figure 2-a, b). This loss was correlated with the formation of inorganic SEI decomposition products including LiF (from ^{19}F and ^{7}Li ssNMR) (Figure 4); only negligible quantities of organic species, associated with residual DMC and EC and their decomposition products, were detected using ^{13}C ssNMR. Li_2CO_3 was not detected by ^{13}C ssNMR in either of the ^{13}C-labeled samples, indicating that if present, it was below the detection limit of the experiment. The results are in stark contrast to the binder-free electrode system, where more significant organic SEI formation after the first cycle was seen,[23] indicating that the CMC binder in the composite system inhibits organic SEI formation and capacity loss. On the basis of the electrochemistry of the conductive C (Figure 3), some of the irreversible capacity loss of the first cycle of the Si composite electrode is ascribed to SEI growth on the surfaces of the conductive C particles, where a current dependent lithiation capacity loss of approximately 200−300 $mAhg^{-1}$ was observed. The result implies that different electrode formulations, with varying ratios of conductive C to active material, may result in some variation in irreversible capacity loss and SEI formation.

In interval 1, we observed a rapidly declining slippage rate from cycle index 1−3 followed by a steady rate of slippage from cycle index 4−30 (Figure 2c). The two characteristic electrochemical signatures for a-Li_xSi and a-$Li_{(x+x')}Si$ phase formations (with x and x' having values of approximately 2.0 and 1.5),[38] initially occurring at 250 and 100 mV, were clearly seen in the differential capacity curves (Figure 2d). The first process is associated with the breakup of the a-Si network, to form larger clusters, while the second involves the formation of small clusters such as Si−Si dimers and eventual isolated Si anions.[39] With Li being accommodated in the structure of Si, repeated Si-particle expansion and contraction occur during each cycle, illustrated schematically in Figure 9a.[17] The expansion likely results in cracking in the SEI formed on the Si particle surfaces resulting in (i) additional Li^+ ion diffusion pathways to access the Si particles, in addition to the diffusion pathways through the SEI, and (ii) fresh surfaces for SEI formation (see Figure 9a, left). The SEI growth in this interval was monitored by ssNMR and FIB/SEM (Figures 4 and 8). Using ^{7}Li ssNMR, we confirmed an increasing quantity of Li salts (see Figure 9a, right). These Li-environments included LiF (detected by $^{7}Li/^{19}F$ ssNMR), Li_2CO_3, HCO_2Li, RCO_2Li, and $ROCO_2Li$ (detected by $^{7}Li/^{13}C$ ssNMR). The ^{13}C results clearly demonstrated that the SEI growth was largely due to the decomposition of the organic electrolytes (EC and DMC). Only a minor increase in the amount of LiF in the SEI was observed, showing negligible decomposition of $LiPF_6$ and resulting reactions forming LiF. The result is in agreement with a previous ssNMR study of a Si composite electrode Li-ion system that also detected negligible increases in the quantity of LiF over multiple cycles.[47] The FIB/SEM analysis (Figure 8) showed surface layers on the C and Si particles which were attributed to SEI formation based on the chemical information from the ssNMR. An increased electrode density was attributed to particle agglomeration and SEI build-up within the bulk of the electrode.

The chemical composition of the SEI organics was investigated in detail for the 30 cycle samples, the composition dictating SEI elasticity (and therefore growth) and Li^+ ion transport from the electrolyte to the Si particles. By ^{13}C ssNMR correlation and CP experiments (Figures 5 and 6), we confirmed our assignment of specific resonances to organic oligomer fragments and aliphatic groups in disordered/amorphous environments in the SEI. These environments gave rise to broad resonances from functional groups such as RCH_2R', CH_3R, and CH_3CH_2R products that arise from radical (including proton abstraction) reactions of the initial EC and DMC decomposition products. Our previous study of the first lithiation reaction,[23] suggested that these reactions occur at lower voltages (<250 mV). Correlation ssNMR experiments in this study (Figure 5b) confirmed chemical bonding between these aliphatic functional groups and CH_2O groups in the ^{13}C-labeled EC sample, providing strong evidence for the presence of SEI molecules such as LBDC, LEC, and RCO_2Li. In addition, at least two different $-OCH_2CH_2O-$ fragments contained in oligomers and/or $ROCO_2Li$ salts were observed (Figure 5c). Analogous ssNMR experiments on the ^{13}C-labeled DMC sample supported the presence of LMC. Similar organic environments were detected in our previous study of a binder-free C/Si electrode,[23] indicating strong similarities between the SEI composition of 1-cycle binder-free electrodes and the multicycled composite electrodes investigated in this study. Of note, the thicker SEI formed here resulted in increased overall ^{13}C ssNMR signal intensity, improving the sensitivity of the NMR experiment, allowing, for example, the length and composition of the alkyl chains of the SEI organics (Figures 5 and 6) to be analyzed by investigating correlations in the 0−70 ppm region of the ^{13}C ssNMR spectra. These ^{13}C correlation experiments are not practicable on samples with insufficient SEI or with samples prepared with natural abundance ^{13}C electrolytes. Note that even under the current conditions, the experiments still required 321 h of continuous acquisition on a high field NMR instrument, emphasizing the challenges in characterizing these nanoscale thick interfaces. Interestingly, LiOH was detected in the multicycled composite electrode system here (see the Supporting Information) compared to our previous study of a binder-free electrode system where no LiOH was detected.[23] The most likely explanation for this is that the CMC binder is difficult to dry completely, introducing trace water into the pristine electrode system. The experimental results here confirm the types of organics contained in the SEI, the decomposition mechanisms of EC and DMC being proposed and debated in the literature.[3,6,21,40,48−53] Furthermore, the results provide a baseline for which to explore ways to enhance SEI properties and stabilize its growth in the early stages of cycling. Future work will incorporate electrolyte additives to investigate experimentally why additives improve capacity retention in these systems.

On interval 2 (from cycle 30 to 60), we observed a declining rate of slippage (see Figure 2c), compared with a steady slippage rate on interval 1. To a first approximation, the SEI thickness had stabilized, a quantitative analysis of the ^{13}C ssNMR (Figure 4) signal intensities showing evidence for only a minor increase of approximately 10−20%. The FIB/SEM (Figure 8) results indicated only minor differences between the morphologies of the cycle 30 and cycle 60 electrodes, the results suggesting some evidence for the presence of fewer smaller pores in the cycle 60 sample compared with the cycle

DOI: 10.1021/jacs.6b02882
J. Am. Chem. Soc. 2016, 138, 7918−7931

30 sample. The smaller lithiation capacity of the electrodes in interval 2 results in significantly reduced expansion and contraction of the electrodes during cycling, leading to less crack formation in the SEI, the creation of fewer new Li^+ ion diffusion pathways through the SEI, and fresh Li_xSi surfaces. We therefore ascribe the negligible SEI growth during interval 2, and declining slippage rate, at least in part to this reduced expansion/contraction. Nonetheless, the electrode lithiation capacity continues to decrease. Since the amount of available Li metal in the half cell is large (approximately 23 mg) compared to the Li consumed irreversibly, the consumption of Li metal is not a clear factor in the cell failure. The availability of sufficient Li metal was experimentally confirmed; see the Supporting Information. However, the presence of side reactions on the Li metal counter electrode has not been accounted for in our analysis. Mechanical failure in the electrodes is clearly evident, with cracking through the electrode structure observed by SEM (Figure 7), which may result in electrically inactive areas of the electrode. However, a pronounced growth in the quantity of trapped Li silicides in interval 2 is not evident in our quantitative ^{7}Li ssNMR results, trapped Li silicides leading to a larger increase in the signal intensity. Interestingly, of the two characteristic a-Li_xSi and a-$Li_{(x+x')}Si$ processes of amorphous Si, a large drop in capacity is seen for the higher voltage process, initially occurring at 250 mV, in interval 2 (Figure 2c). This reduced capacity is seen for both lithiation and delithiation (discharge and charge), indicating that the change in the electrochemistry was symmetric.

The increase in signal intensities measured by ssNMR is noticeably smaller than predicted on the basis of the endpoint slippages Δ_1/Δ_2 (see Figure 2a, b), assuming all the slippage is due to inorganic or organic SEI formation. Furthermore, no new chemical environments are detected between 30 and 60 cycles, in any of the ssNMR spectra. This suggests that additional factors beyond SEI growth contribute to the endpoint slippage. For example, soluble SEI products contained in the electrolyte[46] have not been accounted for in this ssNMR study.

In contrast with the voltage limited cycling used in this study, two key studies that have investigated the role that SEI formation plays in capacity loss have used capacity limited cycling.[13,14] In capacity limited cycling, the low voltage limit steadily decreases on cycling, as Li is consumed in the formation of the SEI (and in other irreversible processes), while the discharge capacity in each cycle is held constant. Generally, following the seminal paper by Obvrovac,[15] the capacity limited cycling is thought to occur via the reaction of Li with the outer shell of the crystalline Si particles, resulting in an outer amorphous Si shell and a crystalline core. Eventually, as the voltage limit decreases on cycling, all of the crystalline Si core is lithiated. At this point, rapid cell failure occurs. For example, Radvanyi et al.[13] showed a rapid failure process after approximately 50 electrochemical cycles with a capacity of 1200 $mAhg^{-1}$; this occurred when the cell lower voltage limit had dropped from its initial value of 200 mV in the first cycle to 30 mV. Similarly, Oumellal et al.,[14] also observed a rapid failure process at approximately 90 cycles when their voltage limit dropped from 100 to 5 mV (initially cycling near 100 mV due to their capacity limit of 1200 $mAhg^{-1}$). The exact failure mechanisms seen under this cycling regime may differ somewhat than the mechanisms relevant to our study because the mechanical stresses, and the time spent at low potentials differ: (i) the stresses associated with the lithiation of the crystalline core in the capacity limited cycling are very different than the lithiation of the more homogeneous amorphous silicon particles in the voltage limited cycling in this study, (ii) we have shown that different degradation processes and different SEI products form on cycling down to the low voltage limit.[23] Despite these differences, reduced Li^+ ion diffusion through the electrode and through the SEI appears to be a failure mode when using both methods. Oumellal et al.[14] present a model where SEI build-up in the pores of the electrode increase the tortuosity of the electrode. Radvanyi et al. present a model for failure that shows a Li^+ ion concentration gradient across the electrode, where the electrode is preferentially lithiated at the top of the electrode, next to the separator (i.e., the reaction is limited by the flux of Li^+ ions), due to the lithium transport being impeded through the bulk of the electrode.[13]

An extension to these Si electrode failure models is presented in Figure 9. SEI growth on particle surfaces due to the large volume expansion associated with Si-particle lithiation is captured schematically in Figure 9a.[17] Delamination of the SEI into the pores of the electrode, coupled with the mechanical stresses and particle agglomeration, result in the increased electrode density confirmed by FIB/SEM. In the early stages of cycling, Li^+ ions can access the entire porous electrode structure, described in Figure 9b, left. Consequently, the capacity associated with both the characteristic a−Li_xSi and a−$Li_{(x+x')}Si$ processes is achieved, and continuous volume expansion and contraction result in pronounced SEI growth, which we confirmed by ssNMR (Figure 4). The dense electrode structure and increased tortuosity seen at later stages of cycling likely impedes Li^+ ion diffusion through the bulk of the electrode, described schematically in Figure 9b, right. In this end failure mode, the decreasing capacity associated with the higher voltage Li_xSi (250 mV) process, Figure 9c, coupled with the SEI stabilization confirmed by ssNMR and FIB/SEM, strongly support a model where Li^+ ion diffusion is limited to surface regions of the electrode. These accessible surface regions are likely located near the electrolyte saturated separator and/or to surface regions of the large voids that may still be accessible deeper inside the electrode, nearer to the current collector. In this surface-limited diffusion model, the reaction will still occur sequentially, first via the higher voltage (250 mV) process, breaking apart the a-Si network to form a-Li_xSi. It is then kinetically more facile for the lithium ions to continue to react with the a-Li_xSi network to form a-$Li_{(x+x')}Si$, than for the Li^+ ions to diffuse further into the electrode. This will result in a front of a-$Li_{(x+x')}Si$ that moves through the electrode, from the separator to the current collector, and from the surface of the agglomerated particles into the center. Furthermore, it will be associated with the electrochemical signature of the second process. This has analogies with the first lithiation of crystalline Si, where the reaction proceeds at approximately 100 mV to form a mixture of small Si dimers and isolated Si.[10] The large volume expansion associated with this a-$Li_{(x+x')}Si$ phase formation is expected to further impede Li^+ ion diffusion through the bulk of the electrode (see Figure 9b, right, bottom). Inaccessible Si results in further lithiation capacity loss and decreased volume expansion of the electrode. The decreased volume expansion would then reduce the SEI cracking and number of fresh surfaces for which to form more SEI, in agreement with the decreased SEI growth detected on interval 2 by ssNMR. By cycle 60, the higher voltage (a-Li_xSi, 250 mV) Si process is absent, indicating that

DOI: 10.1021/jacs.6b02882
J. Am. Chem. Soc. 2016, 138, 7918−7931

the thickness of the surface layer and amount of accessible Si continues to decrease in the end-failure mode. The relationship between Li^+ ion diffusion concentration gradients, electrode porosity, and tortuosity, are well-known; for example, we have previously investigated inhomogeneous electrochemical reactions through porous $LiFePO_4$ electrodes using in situ energy-dispersive X-ray diffraction.[54] In the study, simulations showed that reducing electrode porosity from 35% to 15%, resulted in Li^+ ion concentration gradients (Li fraction/mm) that increased by a factor of approximately 2−3, depending on active material particle size distributions. These concentration gradients then resulted in inhomogeneous particle reactions across the electrode. With the porosity of the Si electrodes in this study dramatically decreasing during repeated cycling, Li^+ ion concentration gradients are reasonably expected to have a significant impact on the kinetics of the system.

CONCLUSIONS

Si electrode failure was investigated by cycling Si/CMC/C composite Si electrodes at their full capacity, between the voltage potential limits of 1 mV and 2 V, at a constant current. The SEI growth, formed from the reduction of a standard 1 M $LiPF_6$ in EC/DMC electrolyte, was directly measured and quantified using ^7Li, ^{19}F, and ^{13}C ssNMR. The accumulation of the SEI in the pores of the electrode was demonstrated by FIB/SEM. In the first cycle, the SEI composition was dominated by inorganic decomposition products, including LiF and additional Li salts. After the lithiation capacity had dropped to only 50% of its initial value, the bulk of the SEI growth had already occurred and significant quantities of organic SEI decomposition products were detected. Using ^{13}C ssNMR correlation experiments, we showed definitive evidence for at least two different $-OCH_2CH_2O-$ fragments, present in $ROCO_2Li$ and oligomeric species. Chemical bonds between CH_2O and functional groups CH_3R, RCH_2R', and CH_3CH_2R were confirmed, showing strong evidence for the presence of LEC, LBDC, and RCO_2Li SEI decomposition products. The presence of HCO_2Li, Li_2CO_3, and LMC, was also confirmed. Interestingly, subsequent cycling and degradation, down to a 20% lithiation capacity of the electrode, was not correlated with significant SEI growth or a significant evolution in the chemical composition. Furthermore, no clear electrode structure changes were evident by FIB/SEM. The decreasing rate of lithiation endpoint slippage correlates with less Si being lithiated and delithiated at later stages of cycling. Also evident by the electrochemical curves, the kinetics for a-Si particle lithiation had evolved.

Our results support a model for lithiation capacity loss that can be roughly approximated into two stages. In the first stage, the capacity loss is correlated with a growth in the SEI and increasing electrode tortuosity. The increased electrode density observed by FIB/SEM was ascribed to a combination of SEI formation on the Si particles, particle agglomeration, and SEI exfoliation from particle surfaces filling the pores of the electrode. In the second stage, the decreasing lithiation capacity is attributed to kinetics. The results support a model where Li^+ ion diffusion is severely limited by the increased electrode tortuosity through the bulk of the electrode. Surface-limited diffusion is reflected in the electrochemistry, which shows a steadily decreasing measured capacity from the process typically associated with Li_xSi ($x \sim 2.0$) formation.

ASSOCIATED CONTENT

Supporting Information

The Supporting Information is available free of charge on the ACS Publications website at DOI: 10.1021/jacs.6b02882.

Further FIB/SEM/TEM electrode characterization and ssNMR experimental details and spectra (PDF)

AUTHOR INFORMATION

Corresponding Author

*cpg27@cam.ac.uk

Notes

The authors declare no competing financial interest.

ACKNOWLEDGMENTS

This work was partially supported by the Assistant Secretary for Energy Efficiency and Renewable Energy, Office of Vehicle Technologies of the U.S. Department of Energy under Contract No. DE-AC02-05CH11231, under the Batteries for Advanced Transportation Technologies (BATT) Program subcontract #7057154 and the European Commission (EC), through the project EuroLion. G.D. and C.D. acknowledge funding from the ERC under Grants 259619 PHOTO EM and 312483 ESTEEM2. A.L.M. is an awardee of a Schiff Foundation Studentship and a nanoDTC Associate. M.L. is an awardee of the Weizmann Institute of Science - National Postdoctoral Award for Advancing Women in Science and thanks the EU Marie Curie intra-European fellowship for funding. We also thank members of the EuroLion Collaboration, Prof. Steven P. Brown (Warwick), and Dr. John M. Griffin (Lancaster) for helpful discussions.

REFERENCES

(1) Peled, E. *J. Electrochem. Soc.* **1979**, *126*, 2047−2051.
(2) Fong, R.; Von Sacken, U.; Dahn, J. R. *J. Electrochem. Soc.* **1990**, *137*, 2009−2013.
(3) Peled, E.; Golodnitsky, D.; Ardel, G. *J. Electrochem. Soc.* **1997**, *144*, L208−L210.
(4) Xu, K. *Chem. Rev.* **2004**, *104*, 4303−4418.
(5) Winter, M. *Z. Phys. Chem.* **2009**, *223*, 1395−1406.
(6) Xu, K.; von Cresce, A. *J. Mater. Chem.* **2011**, *21*, 9849−9864.
(7) Xu, K. *Chem. Rev.* **2014**, *114*, 11503−11618.
(8) Obrovac, M. N.; Christensen, L. *Electrochem. Solid-State Lett.* **2004**, *7*, A93−A96.
(9) Obrovac, M. N.; Chevrier, V. L. *Chem. Rev.* **2014**, *114*, 11444−11502.
(10) Key, B.; Bhattacharyya, R.; Morcrette, M.; Seznéc, V.; Tarascon, J.-M.; Grey, C. P. *J. Am. Chem. Soc.* **2009**, *131*, 9239−9249.
(11) Beaulieu, L. Y.; Eberman, K. W.; Turner, R. L.; Krause, L. J.; Dahn, J. R. *Electrochem. Solid-State Lett.* **2001**, *4*, A137−A140.
(12) Besenhard, J. O.; Yang, J.; Winter, M. *J. Power Sources* **1997**, *68*, 87−90.
(13) Radvanyi, E.; Porcher, W.; De Vito, E.; Montani, A.; Franger, S.; Jouanneau Si Larbi, S. *Phys. Chem. Chem. Phys.* **2014**, *16*, 17142−17153.
(14) Oumellal, Y.; Delpuech, N.; Mazouzi, D.; Dupré, N.; Gaubicher, J.; Moreau, P.; Soudan, P.; Lestriez, B.; Guyomard, D. *J. Mater. Chem.* **2011**, *21*, 6201−6208.
(15) Obrovac, M. N.; Krause, L. J. *J. Electrochem. Soc.* **2007**, *154*, A103−A108.
(16) Chan, C. K.; Peng, H.; Liu, G.; McIlwrath, K.; Zhang, X. F.; Huggins, R. A.; Cui, Y. *Nat. Nanotechnol.* **2008**, *3*, 31−35.
(17) Wu, H.; Chan, G.; Choi, J. W.; Ryu, I.; Yao, Y.; McDowell, M. T.; Lee, S. W.; Jackson, A.; Yang, Y.; Hu, L.; Cui, Y. *Nat. Nanotechnol.* **2012**, *7*, 310−315.

DOI: 10.1021/jacs.6b02882
J. Am. Chem. Soc. 2016, 138, 7918−7931

(18) Aurbach, D.; Gamolsky, K.; Markovsky, B.; Gofer, Y.; Schmidt, M.; Heider, U. *Electrochim. Acta* **2002**, *47*, 1423−1439.
(19) El Ouatani, L.; Dedryvère, R.; Siret, C.; Biensan, P.; Reynaud, S.; Iratçabal, P.; Gonbeau, D. *J. Electrochem. Soc.* **2009**, *156*, A103−A113.
(20) Zhang, S. S. *J. Power Sources* **2006**, *162*, 1379−1394.
(21) Schroder, K. W.; Celio, H.; Webb, L. J.; Stevenson, K. J. *J. Phys. Chem. C* **2012**, *116*, 19737−19747.
(22) Malmgren, S.; Ciosek, K.; Lindblad, R.; Plogmaker, S.; Kühn, J.; Rensmo, H.; Edström, K.; Hahlin, M. *Electrochim. Acta* **2013**, *105*, 83−91.
(23) Michan, A. L.; Leskes, M.; Grey, C. P. *Chem. Mater.* **2016**, *28*, 385−398.
(24) Morcombe, C. R.; Zilm, K. W. *J. Magn. Reson.* **2003**, *162*, 479−486.
(25) Apperley, D. C.; Harris, R. K.; Hodgkinson, P. *Solid State NMR*; Momentum Press: New York, 2012.
(26) Massiot, D.; Fayon, F.; Capron, M.; King, I.; Le Calvé, S.; Alonso, B.; Durand, J.-O.; Bujoli, B.; Gan, Z.; Hoatson, G. *Magn. Reson. Chem.* **2002**, *40*, 70−76.
(27) Thakur, R. S.; Kurur, N. D.; Madhu, P. K. *Chem. Phys. Lett.* **2006**, *426*, 459−463.
(28) Lesage, A.; Bardet, M.; Emsley, L. *J. Am. Chem. Soc.* **1999**, *121*, 10987−10993.
(29) Bax, A.; Freeman, R.; Kempsell, S. P. *J. Am. Chem. Soc.* **1980**, *102*, 4849−4851.
(30) Bax, A.; Freeman, R.; Frenkiel, T. A. *J. Am. Chem. Soc.* **1981**, *103*, 2102−2104.
(31) Cadars, S.; Sein, J.; Duma, L.; Lesage, A.; Pham, T. N.; Baltisberger, J. H.; Brown, S. P.; Emsley, L. *J. Magn. Reson.* **2007**, *188*, 24−34.
(32) Opella, S. J.; Frey, M. H. *J. Am. Chem. Soc.* **1979**, *101*, 5854−5856.
(33) Smith, A. J.; Burns, J. C.; Xiong, D.; Dahn, J. R. *J. Electrochem. Soc.* **2011**, *158*, A1136−A1142.
(34) Iaboni, D. S. M.; Obrovac, M. N. *J. Electrochem. Soc.* **2016**, *163*, A255−A261.
(35) Du, Z.; Hatchard, T. D.; Dunlap, R. A.; Obrovac, M. N. *J. Electrochem. Soc.* **2015**, *162*, A1858−A1863.
(36) Smith, A. J.; Burns, J. C.; Trussler, S.; Dahn, J. R. *J. Electrochem. Soc.* **2010**, *157*, A196−A202.
(37) Li, J.; Dahn, J. R. *J. Electrochem. Soc.* **2007**, *154*, A156−A161.
(38) Ogata, K.; Salager, E.; Kerr, C. J.; Fraser, A. E.; Ducati, C.; Morris, A. J.; Hofmann, S.; Grey, C. P. *Nat. Commun.* **2014**, *5*, 3217.
(39) Key, B.; Morcrette, M.; Tarascon, J.-M.; Grey, C. P. *J. Am. Chem. Soc.* **2011**, *133*, 503−512.
(40) Aurbach, D. *J. Power Sources* **2000**, *89*, 206−218.
(41) MacKenzie, K. J. D.; Smith, M. E. In *Multinuclear Solid-State Nuclear Magnetic Resonance of Inorganic Materials*, 1st ed.; Cahn, R. W., Ed.; Pergamon materials series; Pergamon: Oxford, 2002.
(42) Philippe, B.; Dedryvère, R.; Gorgoi, M.; Rensmo, H.; Gonbeau, D.; Edström, K. *Chem. Mater.* **2013**, *25*, 394−404.
(43) Meyer, B. M.; Leifer, N.; Sakamoto, S.; Greenbaum, S. G.; Grey, C. P. *Electrochem. Solid-State Lett.* **2005**, *8*, A145−A148.
(44) Kim, T.; Park, S.; Oh, S. M. *J. Electrochem. Soc.* **2007**, *154*, A1112−A1117.
(45) Philippe, B.; Dedryvère, R.; Allouche, J.; Lindgren, F.; Gorgoi, M.; Rensmo, H.; Gonbeau, D.; Edström, K. *Chem. Mater.* **2012**, *24*, 1107−1115.
(46) Huff, L. A.; Tavassol, H.; Esbenshade, J. L.; Xing, W.; Chiang, Y.-M.; Gewirth, A. A. *ACS Appl. Mater. Interfaces* **2016**, *8*, 371−380.
(47) Delpuech, N.; Dupré, N.; Mazouzi, D.; Gaubicher, J.; Moreau, P.; Bridel, J. S.; Guyomard, D.; Lestriez, B. *Electrochem. Commun.* **2013**, *33*, 72−75.
(48) Soto, F. A.; Ma, Y.; Martínez de la Hoz, J. M.; Seminario, J. M.; Balbuena, P. B. *Chem. Mater.* **2015**, *27*, 7990−8000.
(49) Aurbach, D.; Zinigrad, E.; Cohen, Y.; Teller, H. *Solid State Ionics* **2002**, *148*, 405−416.
(50) Dedryvère, R.; Laruelle, S.; Grugeon, S.; Gireaud, L.; Tarascon, J. M.; Gonbeau, D. *J. Electrochem. Soc.* **2005**, *152*, A689−A696.
(51) Nie, M.; Chalasani, D.; Abraham, D. P.; Chen, Y.; Bose, A.; Lucht, B. L. *J. Phys. Chem. C* **2013**, *117*, 1257−1267.
(52) Tavassol, H.; Buthker, J. W.; Ferguson, G. A.; Curtiss, L. A.; Gewirth, A. A. *J. Electrochem. Soc.* **2012**, *159*, A730−A738.
(53) Wang, Y.; Nakamura, S.; Ue, M.; Balbuena, P. B. *J. Am. Chem. Soc.* **2001**, *123*, 11708−11718.
(54) Strobridge, F. C.; Orvananos, B.; Croft, M.; Yu, H.-C.; Robert, R.; Liu, H.; Zhong, Z.; Connolley, T.; Drakopoulos, M.; Thornton, K.; Grey, C. P. *Chem. Mater.* **2015**, *27*, 2374−2386.

DOI: 10.1021/jacs.6b02882
J. Am. Chem. Soc. 2016, 138, 7918−7931